Experimental and numerical investigations on wave dynamics of a dual-chamber OWC wave energy device

Proceedings of the ASME 2019 38th International Conference on Ocean, Offshore and Arctic Engineering
OMAE2019
June 9-14, 2019, Glasgow, Scotland

OMAE2019-95165

EXPERIMENTAL AND NUMERICAL INVESTIGATIONS ON WAVE DYNAMICS OF A DUAL-CHAMBER OWC WAVE ENERGY DEVICE

Dezhi Ning[1,2,*], Rongquan Wang[1,2], Bin Teng[1,2]

[1] State Key Laboratory of Coastal and Offshore Engineering, Dalian University of Technology, Dalian 116024, China
[2] Offshore Renewable Energy Research Center, Dalian University of Technology, Dalian 116024, China

Qingping Zou[3]

[3] The Lyell Centre for Earth and Marine Science and Technology, Institute for Infrastructure and Environment, Heriot-Watt University, Edinburgh, EH14 4AS, UK

ABSTRACT

Oscillating Water Column (OWC) wave energy device is one of the most studied and applied wave energy converters (WECs). The survivability of WECs is a major concern in the OWC design. In this study, the wave dynamics of a dual-chamber OWC device is numerically and experimentally investigated. The experimental tests were carried out in the wave-current flume at the State Key Laboratory of Coastal and Offshore Engineering, Dalian University of Technology. A fully nonlinear numerical wave flume based on potential-flow theory and time-domain higher-order boundary element method (HOBEM) is developed and applied to simulate the interaction between air, wave and the dual-chamber OWC device. The numerical model is validated by comparing the simulated wave induced pressure on the barrier walls with the measurements. Then the wave forces and the moment on the device is numerically investigated. The model and experimental results indicate that the horizontal wave force on the front barrier wall is much larger than that on the internal barrier wall. The joint between the back wall and the ground withstands the largest bending moment, therefore, is most vulnerable to structure damage and fatigue.

Keywords: OWC; Wave Energy Converter; Wave force; Physical test; HOBEM.

1. INTRODUCTION

As one of the most promising wave energy converter (WEC), the Oscillating Water Column (OWC) has been widely studied in the past few decades [1]. Previous studies mainly focus on improving the hydrodynamic efficiency of the OWC device. Accordingly, the concept of dual-chamber OWC device was proposed to improve the hydrodynamic efficiency recently [2-4]. The survivability of the device is the most important consideration in the design process. However, this has not attracted enough attentions. There are few studies considering the wave force on floating type OWC device [5-9]. While for the fixed type OWC device, the related research is even more scarce. Ashlin et al. [10] experimentally investigated the effects of wave steepness and relative water depth on wave forces on the device. Ning et al. [11] numerically and experimentally investigated the effects of the wave conditions and chamber geometry on the wave force on the front wall of the OWC device. However, the survivability of the device remains a major issue in the field operation of WECs. Both the most powerful bottom-standing wave energy devices constructed so far, the OSPREY in Scotland and the green WAVE in Australia, were destroyed in the disastrous deployment operations, in 1995 and 2014 respectively [12]. The concrete subsurface structure of the Pico plant in Portugal was severely damaged by waves [13] and the plant partially collapsed during a strong sea storm on 17th April 2018 [14]. Thus, both the wave force and the bending moment exerts to the device should be accounted for.

The dual-chamber OWC device can achieve a higher maximum efficiency and a wider effective frequency bandwidth when compared to an equivalent typical single-chamber OWC device [15]. Thus, in the present paper, the wave dynamics of a dual-chamber device is numerically and experimentally

* Contact author: dzning@dlut.edu.cn

investigated with special attentions paid to the wave forces on the two barrier and the moment applied to the structure.

2. NUMERICAL MODEL

The schematic of the numerical wave flume is shown in Fig. 1. A Cartesian coordinate system *Oxz* is defined with its origin *O* on the still water surface and the *z*-axis pointing upward. As shown in Fig. 1, B_1 and B_2 are the breadths of the chamber 1 and chamber 2, B_{O1} and B_{O2} are the widths of the orifices of the chamber 1 and chamber 2, C_1 and C_2 are the thicknesses of the barrier wall 1 and barrier wall 2,; d_1 and d_2 are the drafts of the barrier wall 1 and barrier wall 2, L_d is the length of the sponge layer, h is the static water depth and h_c is the height of the air chambers above the still water surface, Γ is the computational boundary, including Γ_{fO}, Γ_{fc1}, Γ_{fc2} and Γ_b

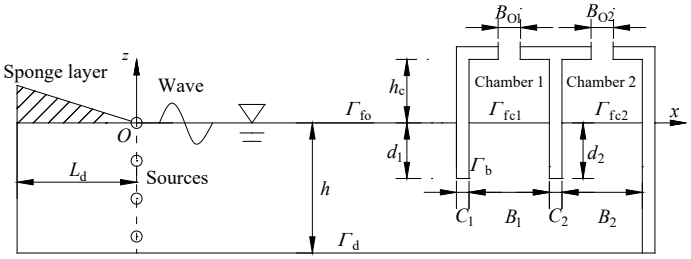

FIGURE 1: Schematic of the numerical wave flume.

The fluid motion can be described by the velocity potential ϕ, which is relating with the fluid velocity, by assuming that the fluid is inviscid, incompressible, and the fluid flow is irrotational. In the numerical model, the inner sources method is used to generate incident wave. To avoid the re-reflection, the sponge layer with coefficient $\upsilon(x)$ is implemented at the left end of the numerical wave flume to absorb the reflected waves. To account for the energy loss due to the flow separation and the vortex shedding around the OWC device, an artificial viscous damping term with coefficient μ is applied to the dynamic free surface boundary condition [11, 16]. Therefore, the fully nonlinear free surface boundary conditions can be expressed as follows:

$$\begin{cases} \dfrac{\mathrm{d}X(x,z)}{\mathrm{d}t} = \nabla\phi - \upsilon(x)\left(X - X_0\right) \\ \dfrac{\mathrm{d}\phi}{\mathrm{d}t} = -g\eta + \dfrac{1}{2}\left(\nabla\phi\cdot\nabla\phi\right) - \dfrac{p_{a(1,2)}}{\rho} - \upsilon(x)\phi - \mu_{(1,2)}\dfrac{\partial\phi}{\partial n} \end{cases}, \tag{1}$$

where $\mathrm{d}/\mathrm{d}t = \partial/\partial t + \nabla\phi\cdot\nabla$ is the material derivative, X_0 $(x_0, 0)$ the initial static position of the fluid particle and $X(x, z)$ the position vector of a fluid particle on the free surface, ϕ the velocity potential, η the wave surface elevation, g the gravity acceleration, ρ the water density and t the time. The artificial viscous damping coefficients $\mu_{(1,2)}$ are determined by trial and error method by comparison with the experimental data and are implemented in chamber 1 and chamber 2. p_a is the air pressure implemented on the free surface. The atmospheric pressure is set to be zero. Thus, p_a is equal to zero outside the chamber, while inside the chamber, p_a is the pneumatic pressure which is due to the motion of the free surface elevation in the chambers. By assuming the quadratic relationship between the pneumatic pressure and the air flow velocity through the orifice, the air pressure can be expressed as follows:

$$p_{a(1,2)}(t) = CD_{dm(1,2)}\left|U_{d(1,2)}(t)\right|U_{d(1,2)}(t) \tag{2}$$

where $CD_{dm(1,2)}$ are the quadratic pneumatic damping coefficients of the chamber 1 and chamber 2 respectively; $U_{d(1,2)}$ are the air flow velocities through the air orifices of chamber 1 and chamber 2, respectively. Based on the assumption of negligible spring-like effect of air compressibility inside the chambers, the air flow velocity U_d can be expressed as follows:

$$U_{d(1,2)}(t) = \frac{\Delta V_{1,2}}{S_{0(1,2)}\Delta t} \tag{3}$$

where $\Delta V_{1,2} = \Delta V_{t+\Delta t(1,2)} - \Delta V_{t(1,2)}$ represent the change of air volume in chamber 1 and chamber 2 within each time step Δt, respectively, which can be calculated with the variation of the free surfaces in the two chambers; $S_{0(1,2)}$ are the cross-sectional area of the air orifice 1, and 2, respectively.

On solid boundaries, including the flume bottom and surface of the OWC device, the zero normal velocity condition is satisfied:

$$\frac{\partial\phi}{\partial \boldsymbol{n}} = 0 \tag{4}$$

where $\boldsymbol{n}$ is the normal direction of the solid boundary with its positive direction point to the solid body.

To solve the proposed boundary value problem in the time domain, the initial conditions are given as

$$\phi\big|_{t=0} = \eta\big|_{t=0} = 0\,. \tag{5}$$

By applying Green's second identity to the fluid domain Ω, the proposed boundary value problem can be converted into the following boundary integral equation:

$$\alpha(p)\phi(p) = \int_{\Gamma}\left[\phi(q)\frac{\partial G(p,q)}{\partial n} - G(p,q)\frac{\partial\phi(q)}{\partial n}\right]\mathrm{d}\Gamma + \int_{\Omega} q^{*}G(p,q)\,\mathrm{d}\Omega\,, \tag{6}$$

where Γ is the computational boundary, including Γ_{fO}, Γ_{fc1}, Γ_{fc2} and Γ_b as indicated in figure 1 p and q represent the source point (x_0, z_0) and the field point (x, z), respectively, and α is the solid angle coefficient determined by the surface geometry at a source point position. G is the simple Green function.

Once Eq. (6) is solved, the velocity potential on the body surface is known. Then the pressure can be obtained from the Bernoulli equation, and the wave force $\boldsymbol{F}$ and moment $\boldsymbol{M}$ on the OWC device can be calculated from the following integration of the transient wave pressure over the wetted surface of the wall (Γ_b) as

$$\boldsymbol{F} = \int_{\Gamma_b} p_w \boldsymbol{n}\,\mathrm{d}\Gamma = -\rho\int_{\Gamma_b}\left[\frac{\partial\phi}{\partial t} + g\eta + \frac{1}{2}\left(\nabla\phi\cdot\nabla\phi\right) + \frac{p_a}{\rho} - \mu\frac{\partial\phi}{\partial t}\right]\boldsymbol{n}\,\mathrm{d}\Gamma\,, \tag{7}$$

$$\boldsymbol{M} = \int_{\Gamma_b} p_{\mathrm{w}} (\boldsymbol{r} \times \boldsymbol{n}) \mathrm{d}\Gamma =$$
$$-\rho \int_{\Gamma_b} \left[\frac{\partial \phi}{\partial t} + g\eta + \frac{1}{2}(\nabla\phi \cdot \nabla\phi) + \frac{p_a}{\rho} - \mu \frac{\partial \phi}{\partial t} \right] (\boldsymbol{r} \times \boldsymbol{n}) \mathrm{d}\Gamma , \quad (8)$$

where p_{w} is the hydrodynamic pressure on the wetted surface, $\boldsymbol{n}$ is the unit vector in the direction of the hydrodynamic pressure, $\boldsymbol{r}$ is the position vector with its direction point from the rotation center to the point where the hydrodynamic pressure is applied. The acceleration-potential method is adopted here to calculate the time derivative of the potential.

3. EXPERIMENTS

The experiments were carried out in the wave-current flume at State Key Laboratory of Coastal and Offshore Engineering, Dalian University of Technology, China. The wave flume is 69 m long, 2.0 m wide and 1.8 m deep. The flume is equipped with a piston-type unidirectional wave-maker at one end and a wave-absorbing beach at the other end to generate and absorb waves, respectively. A thin vertical wall was installed along the longitudinal direction of the flume to divide the flume into two parallel sections with a width of 1.2 m and 0.8 m, respectively. A 1/20 scaled dual-chamber OWC model was installed in the narrower section, spreading across the whole width of the section, to ensure a two-dimensional (2-D) testing condition.

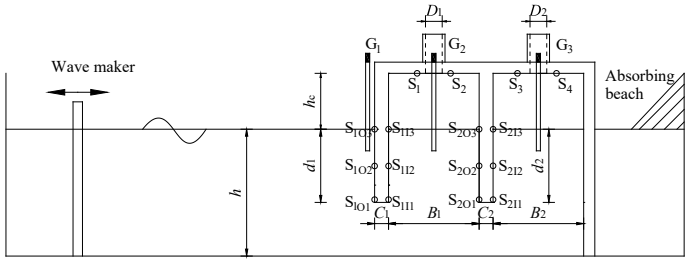

FIGURE 2: Schematic of the experimental setup.

The schematic of the experimental setup is shown in Fig. 2. The dual-chamber OWC model was placed 50 m (about 8-30 times of the wavelength) away from the wave-maker. The chamber breadths were $B_1 = B_2 = 0.325$ m, the thickness of the two barrier walls C was 0.05 m, the barrier wall drafts $d_1 = d_2 = 0.2$ m and the chamber height h_c was 0.2 m. A fixed optimized opening ratio of $\alpha = S/S_0 = 0.66\%$ (where S and S_0 are the cross-sectional areas of the orifice and the air chamber, respectively) for both orifices was used [17]. Accordingly, the diameters of the two orifices were $D_1 = D_2 = 0.045$ m. As shown in Fig. 2, three wave gauges were used to measure the surface elevation at the position, i.e., gauge G_1 at the position 2 cm away from the dual-chamber, gauges G_2 and G_3 are at the mid-points of chamber 1 and chamber 2. Four pressure sensors were fixed at the ceiling of the chambers to measure the air pressure in the chambers (i.e., S_1 and S_2 for chamber 1, and S_3 and S_4 for chamber 2, respectively). To measure the hydrodynamic pressures on the two barrier walls, six pressure sensors, S_{101} to S_{213} were symmetrically and evenly distributed on the surface of each wall and from the bottom edge of the wall to the still water surface.

In this study, periodic regular waves with varying wave periods were generated in a water depth of 1.0 m. In total, 12 incoming waves that have a wave period T ranging from 1.0 s to 2.3 s, and a constant wave amplitude A_i of 0.03 were tested.

4. RESULTS AND DISCUSSIONS

To investigate the wave forces on the dual-chamber OWC device, the validation of the numerical model is carried out firstly. In the numerical model, the orifice widths are chosen as $B_{O1} = B_{O2} = 2.145$ mm, which is equivalent to the area of the circular shaped orifices in the experiments. The other geometric parameters of the dual-chamber are the same as that in the experiments. The viscous coefficients in chamber 1 and chamber 2 are chosen as $\mu_1 = 0$ and $\mu_2 = 0.15$, respectively. The quadratic pneumatic coefficients are chosen as $CD_{\mathrm{dm1}} = CD_{\mathrm{dm2}} = 1.0$. The viscous coefficients and pneumatic coefficients are determined by trial and error method by comparison with the experimental. For a detailed description of this procedure, the reader is referred to [17]. In all cases, after the convergent tests, there are 30 mesh segments per wave length on the free surface, 15 mesh segments are distributed on each barrier wall surface, and 10 mesh segments are used across the depth of the numerical wave flume. For each case, 30 wave periods are simulated with a time step of $\Delta t = T/80$.

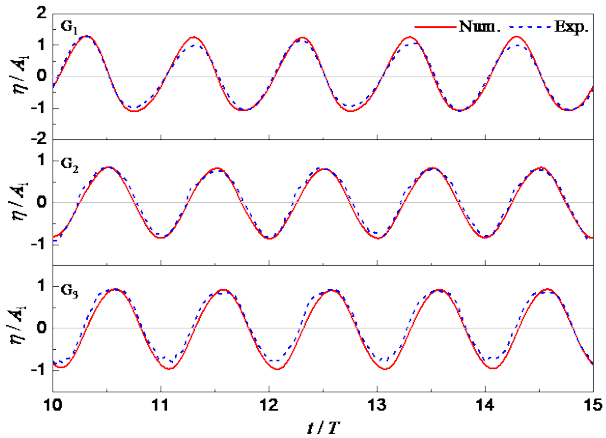

FIGURE 3: Time series of the observed and predicted free surface elevations at gauge G_1, G_2 and G_3 for wave period T = 1.7 s.

Fig. 3 shows the time series of the free surface elevations at gauge G_1, G_2 and G_3 for wave period T = 1.7 s. The predicted wave surface elevations agree well with the observations. Fig. 4 shows the time series of the hydrodynamic pressure on the surface of the two barrier walls. Although, the numerical model over-predicted the measured pressure by pressure sensors S_{2O3} and S_{213} near still water level, which may be due to the complex interaction between air and water at the free surface. Overall, the predicted and observed hydrodynamic pressures on the barrier wall surfaces compared well with each other. These results

indicate that the numerical model can capture the interaction of the wave and dual-chamber OWC device well.

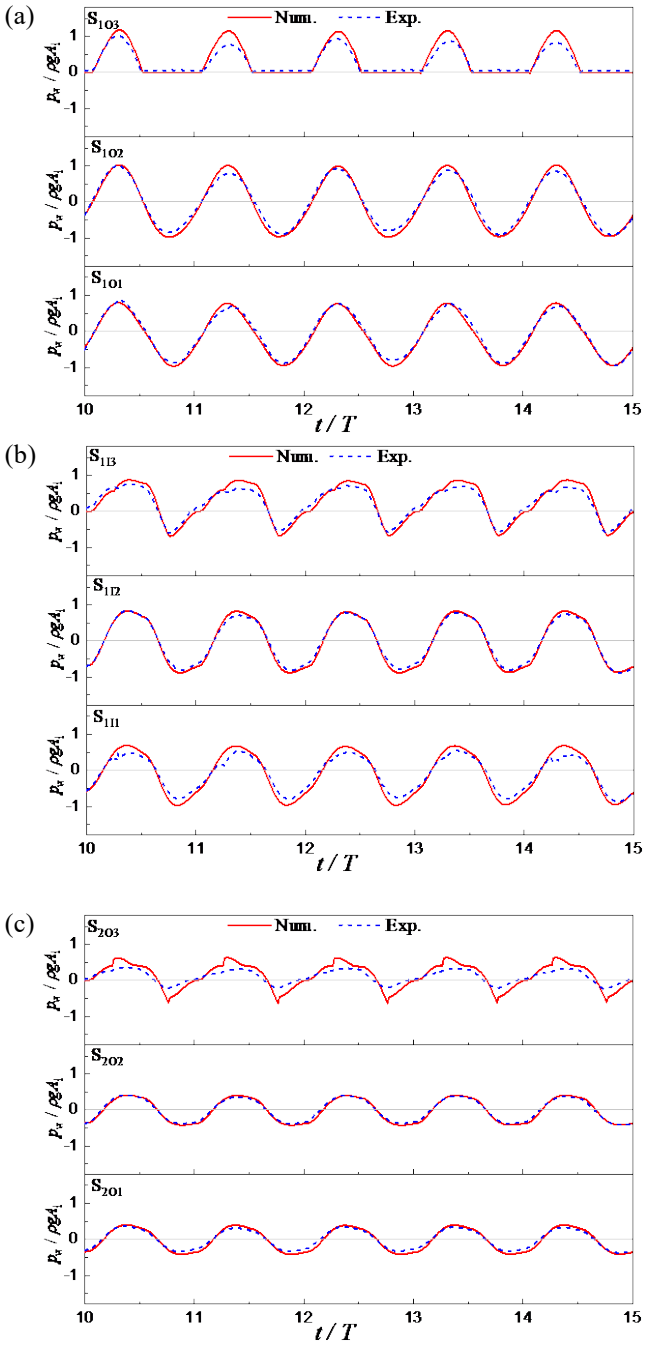

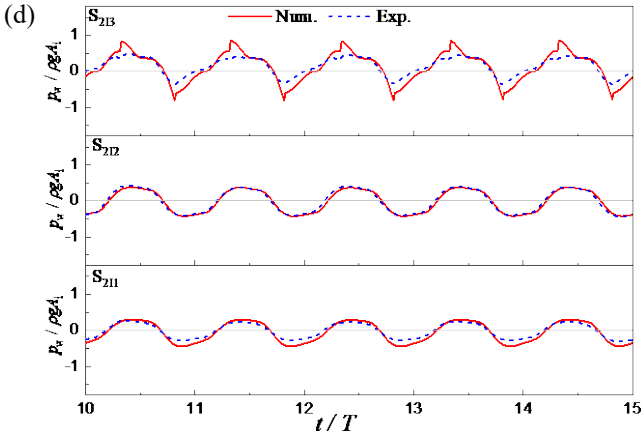

FIGURE 4: Time series of the observed and predicted hydrodynamic pressure on the barrier walls (i.e., S_{1O1} - S_{1O3} (a) and S_{1I1} - S_{1I3} (b) on the two side of the barrier wall 1 and S_{2O1} - S_{2O3} (c) and S_{2I1} - S_{2I3} (d) on the two sides of the barrier wall 2 for wave period $T = 1.7$ s.

The schematic of the wave forces and moments are shown in Fig. 5: (a) points p (p = 1, 2, 3, 4) are the centers of moment; (b) F_{ix} and F_{iz} are the horizontal wave force and vertical wave force on the barrier wall i (i = 1, 2), and F_j is the total wave force on the barrier wall j (j = 1, 2, 4), note that F_4=F_{4x} is the horizontal wave force on the back wall; (c) M_{pj} is the moment about point p due to the total wave force F_j (j = 1, 2, 4); (d) M_p is the total moment about the point p.

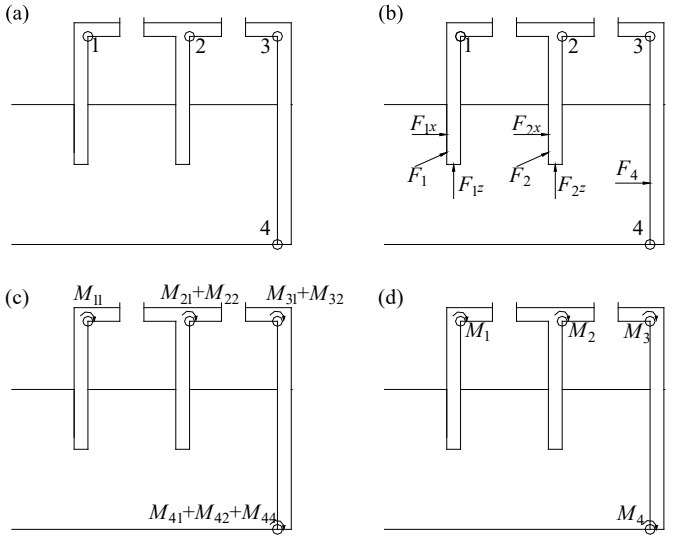

FIGURE 5: (a) Locations of centers of moment, wave forces components; (c) moment components and (d) total moments.

Fig. 6(a) shows the horizontal and vertical wave forces on the two barrier walls. The horizontal wave force on the barrier wall 1, F_{1x}, increases with the wave frequency, while the horizontal wave force on the barrier wall 2, F_{2x}, increases with the wave frequency first to its peak value and then decreases with the wave frequency. Furthermore, Fig 6 indicates that F_{1x} is much

larger than F_{2x}, i.e., most of the horizontal wave forces are exerted on the barrier wall 1, therefore, the barrier wall 1 needs to be reinforced. While the barrier wall 2, does not need to be as strong as barrier wall 1 and may use cheaper building material to save costs. The vertical wave force acting on the barrier walls is much smaller than the horizontal wave forces due to the fact that the bearing areas of vertical force of the barrier walls are smaller (i.e., the thicknesses of the barrier wall is very small).

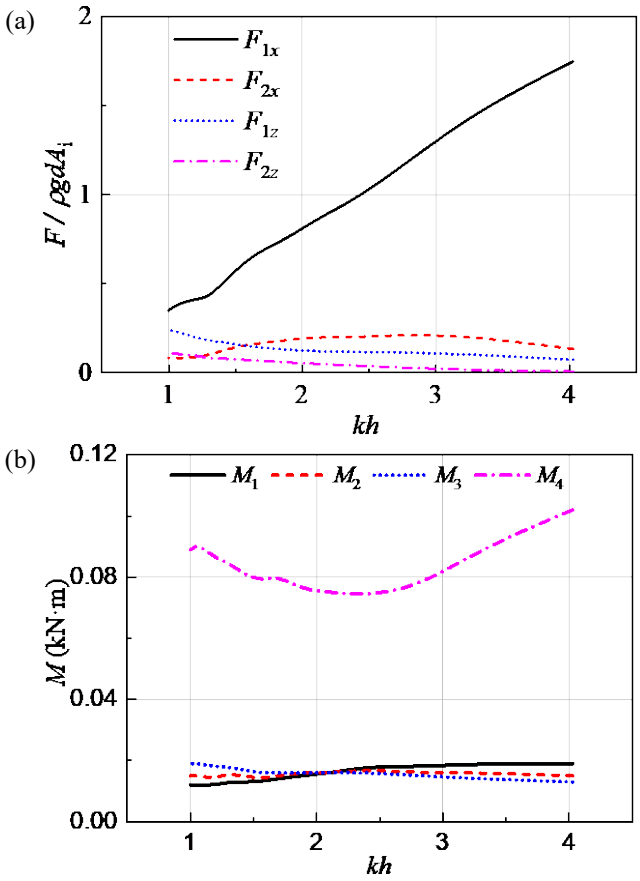

FIGURE 6: Wave forces (a) and moments (b) versus dimensionless wave number kh.

The total moments applied to the four centers of moment indicated in Fig. 5 are shown in Fig. 6(b). It can be observed that the moment about point 4, M_4, is much larger than that about the other three points. This indicates that the joint of the back wall and the ground is the most vulnerable part of the WEC system. To get a better understanding of the mechanism of this phenomenon, the time series of the components of total moment about point 1 to 4 for wave period $T = 1.7$ s are shown in Fig. 7. In the present study, the 2-D OWC model can be simplified as a cantilever structure. Thus, only the wave force on the barrier wall 1, F_1, can exert a moment about center of moment at point 1. Both the wave forces on the barrier wall 1, F_1, and 2, F_2, can apply a bending moment about point 2. As shown in Fig. 7(b), M_{21} is the dominant component of the M_2, namely, the wave force from the barrier wall 1, F_1, contribute the most to the moment about point 2. Similarly, Fig. 7(c) indicates that M_{31} is the dominant component of the M_3, the wave force from the barrier wall 1, F_1, contribute the most to the moment about point 3. For the rotation center 4, both the components M_{41} and M_{44} are important part of the total moment M_4, wave force on Barrier wall 1 and 2 both contribute to M_4, but the former is much larger than the latter.

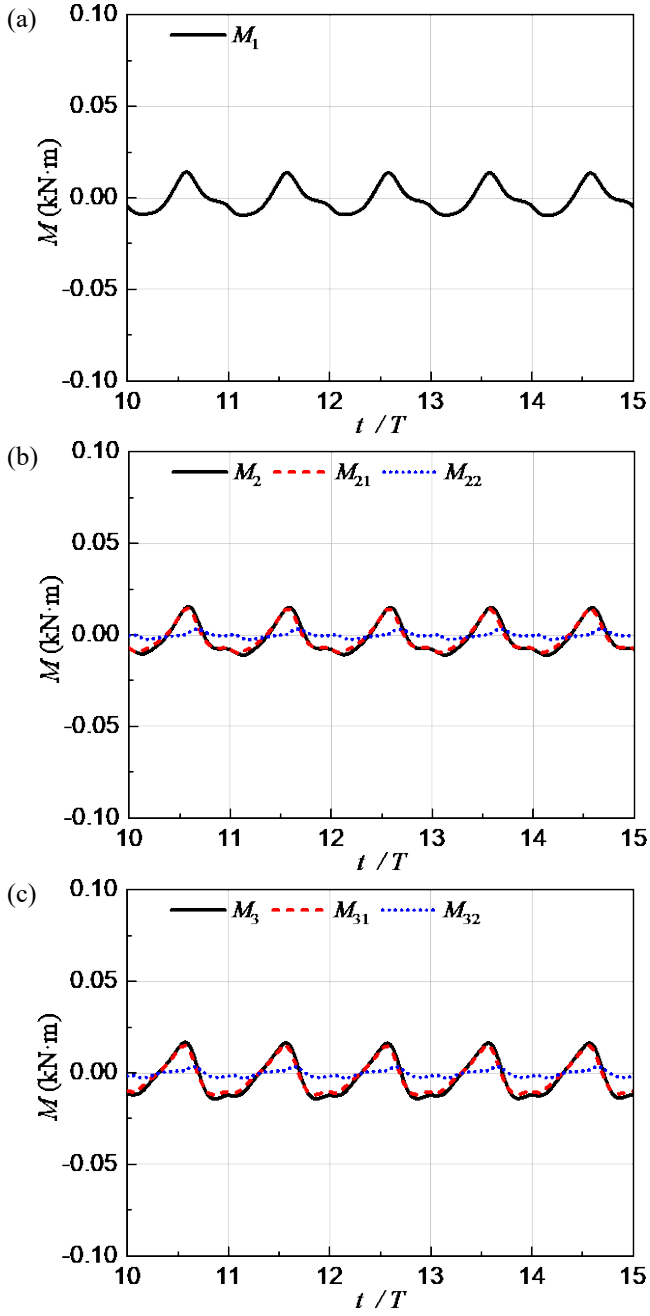

(d)

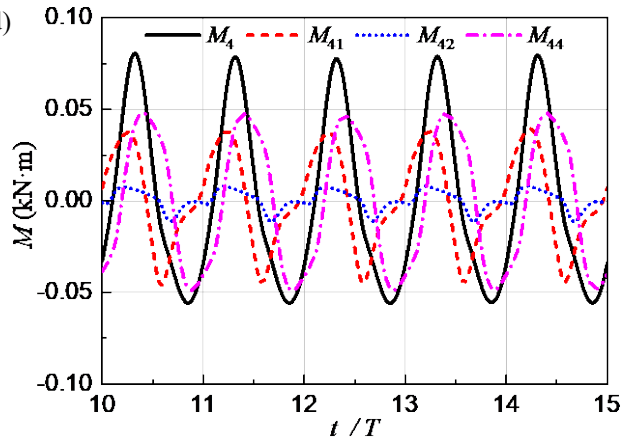

FIGURE 7: Time series of the moments and its components applied to rotation centers for wave period T = 1.7 s.

5. CONCLUSIONS

In the present paper, the wave forces on the dual-chamber device is numerically and experimentally investigated. The 2-D OWC model can be simplified as a cantilever structure. It is found that the horizontal wave force on the barrier wall 1 is much larger than that on the barrier wall 2. The vertical wave force on the barrier wall is much smaller than the horizontal wave force on it. The bending moment at the joint of the back wall and the ground is the largest and the joint is the most vulnerable part of the structure. Thus, it is recommended that the joint is strengthened during the construction of WEC.

ACKNOWLEDGEMENT

This study is supported by the National Science Foundation of China (Grant Nos. 51679036 and 51490672) and the UK-China Industry Academia Partnership Programme (Grant No. UK-CIAPP\73)

REFERENCES

[1] Delauré Y.M.C., Lewis A., 2003. 3D hydrodynamic modelling of fixed oscillating water column wave power plant by a boundary element methods, Ocean Engineering, 30, 309-330.

[2] Rezanejad K., Bhattacharjee J., Soares C.G., 2015. Analytical and numerical study of dual-chamber oscillating water columns on stepped bottom, Renewable Energy, 75, 272-282.

[3] Ning D., Wang R., Zhang C., 2017. Numerical Simulation of a Dual-Chamber Oscillating Water Column Wave Energy Converter, Sustainability, 9, 1599.

[4] Elhanafi A., Macfarlane G., Ning D., 2018. Hydrodynamic performance of single–chamber and dual–chamber offshore–stationary Oscillating Water Column devices using CFD, Applied Energy, 228, 82-96.

[5] Hong D.C., Hong S.Y., Hong S.W., 2004. Numerical study of the motions and drift force of a floating OWC device, Ocean Engineering, 31, 139-164.

[6] Hong D.C., Hong S.Y., Hong S.W., 2004. Numerical study on the reverse drift force of floating BBDB wave energy absorbers, Ocean Engineering, 31, 1257-1294.

[7] Koo W., 2009. Nonlinear time–domain analysis of motion-restrained pneumatic floating breakwater, Ocean Engineering, 36, 723-731.

[8] Konispoliatis D.N., Mavrakos S.A., 2016. Hydrodynamic analysis of an array of interacting free-floating oscillating water column (OWC′s) devices, Ocean Engineering, 111, 179-197.

[9] Elhanafi A., Macfarlane G., Fleming A., Leong Z., 2017. Experimental and numerical investigations on the hydrodynamic performance of a floating–moored oscillating water column wave energy converter, Applied Energy, 205, 369-390.

[10] Ashlin S.J., Sannasiraj S.A., Sundar V., 2015. Wave Forces on an Oscillating Water Column Device, Procedia Engineering, 116, 1019-1026.

[11] Ning D.Z., Wang R.Q., Gou Y., Zhao M., Teng B., 2016. Numerical and experimental investigation of wave dynamics on a land-fixed OWC device, Energy, 115, 326-337.

[12] Falcão A.F.O., Henriques J.C.C., 2016. Oscillating-water-column wave energy converters and air turbines: A review, Renewable Energy, 85, 1391-1424.

[13] Monk K. Forecasting for control and environmental impacts of wave energy converters [Ph.D]: Plymouth University; 2015.

[14] Falcão A., Gato L., Sarmento A., Brito-Melo A. The Pico OWC wave power plant: Its life from conception to closure 1986–2018. Advances in Renewable Energies Offshore: Proceedings of the 3rd International Conference on Renewable Energies Offshore (RENEW 2018). Lisbon, Portugal: CRC Press; 2018. p. 475-483.

[15] Ning D.Z., Wang R.Q., Chen L.F., Sun K., 2019. Experimental investigation of a land-based dual-chamber OWC wave energy converter, Renewable and Sustainable Energy Reviews, 105, 48-60.

[16] Ning D.Z., Shi J., Zou Q.P., Teng B., 2015. Investigation of hydrodynamic performance of an OWC (oscillating water column) wave energy device using a fully nonlinear HOBEM (higher-order boundary element method), Energy, 83, 177-188.

[17] Ning D.Z., Wang R.Q., Zou Q.P., Teng B., 2016. An experimental investigation of hydrodynamics of a fixed OWC Wave Energy Converter, Applied Energy, 168, 636-648.